Journal of Materials Chemistry A

Accepted Manuscript

This article can be cited before page numbers have been issued, to do this please use: F. J. Monzo, Y. Malewski, R. Kortlever, F. J. Vidal-Iglesias, J. Solla-Gullon, M. T.M Koper and P. Rodriguez, *J. Mater. Chem. A*, 2015, DOI: 10.1039/C5TA06804E.

ROYAL SOCIETY OF CHEMISTRY

www.rsc.org/materialsA

View Article Online
DOI: 10.1039/C5TA06804E

Enhanced electrocatalytic activity of Au@Cu core@shell nanoparticles towards CO_2 reduction

J. Monzó [a], Y. Malewski [a], R. Kortlever [b], F. J. Vidal-Iglesias [c], J. Solla-Gullón [c], M.T.M Koper[b] and P. Rodriguez[a]

[a] University of Birmingham, School of Chemistry, Birmingham, B15 2TT, UK.

[b] Leiden Institute of Chemistry, Leiden University, P.O. Box 9502, 2300 RA, Leiden, the Netherlands.

[c] Institute of Electrochemistry, University of Alicante, E-03080, Alicante, Spain.

Corresponding author: p.b.rodriguez@bham.ac.uk

Abstract

The development of technologies for the recycling of carbon dioxide into carbon-containing fuels is one of the major challenges in sustainable energy research. One of the main current limitations is the poor efficiency and fast deactivation of the catalyst. Core-shell nanoparticles are promising candidates for enhancing challenging reactions. In this work, Au@Cu core-shell nanoparticles with well-defined surface structures were synthetized and evaluated as catalysts for the electrochemical reduction of carbon dioxide in neutral medium. The activation potential, the product distribution and the long term durability of this catalyst was assessed by electrochemical methods, on-line electrochemical mass spectrometry (OLEMS) and on-line high performance liquid chromatography. Our results show that the catalytic activity and the selectivity can be tweaked as a function of the thickness of Cu shells. We have observed that the Au cubic nanoparticles with 7-8 layers of copper present higher selectivity towards the formation of hydrogen and ethylene; on the other hand, we observed that Au cubic nanoparticles with more than 14 layers of Cu are more selective towards the formation of hydrogen and methane. A trend in the formation of the gaseous products can be also drawn. The H_2 and CH_4 formation increases with the number of Cu layers, while the formation of ethylene decreases. Formic acid was the only liquid species detected during CO_2 reduction. Similar to the gaseous species, the formation of formic acid is strongly dependent on the number of Cu layers on the core@shell nanoparticles. The Au cubic nanoparticles with 7-8 layer of Cu showed the largest

View Article Online
DOI: 10.1039/C5TA06804E

conversion of CO_2 to formic acid at potentials higher than 0.8V vs RHE. The observed trends in reactivity and selectivity are linked to catalyst composition, surface structure and strain/electronic effects.

Keywords: core shell nanoparticles, CO_2 reduction, electrochemistry, lattice strain.

1. Introduction

The ongoing increases in consumption of fossil fuels and rapid deforestation have caused a dramatic growth of the global concentration of carbon dioxide (CO_2). The 2014 annual greenhouse bulletin of the World Meteorological Organization shows that the levels of CO_2 in the atmosphere in 2013 reached 396.0±0.1 ppm[1] and that the annual increase in the concentration of CO_2 is now higher than 2%. Such unprecedented levels of CO_2 in the atmosphere are causing a drastic impact on both global warming and ocean acidification.

Efforts to decrease the consumption of fossil fuels are very limited, especially since human population and global demand for new and better energy-consuming technologies are rising. In this regard, the capture, fixation and reutilization/valorization of CO_2 have attracted the attention of scientists around the world[2-4]. Electrochemical reduction is one promising alternative for the recycling of CO_2. Even though the electrochemical reduction of CO_2 was reported for the first time by Sir B.C. Brodie in 1873[5] and later in the 1990's by Hori et al.,[6-9] recent discoveries in materials and characterization techniques[3,8,10-20] for the electrochemical reduction of CO_2 have brought renewed focus on this process as a potential solution for CO_2 removal. Hori established in 1986 that bulk Cu electrodes could be used to produce hydrocarbons – CH_4 and C_2H_4 – with efficiencies of 65 % and 20 %, respectively. More recently, Jaramillo's group explored the activity and selectivity of a range of transition metals towards CO_2 reduction. [21] The authors concluded that Au, Ag, Zn, Cu, Ni, Pt, and Fe are capable of producing methane or methanol; some of them are able to produce both.

However in regards to materials being studied for this process, copper (Cu) is still perhaps one of the most interesting metals due to its selective production of hydrocarbons at relatively low overpotential and improved efficiency with respect the other metals. Despite great efforts, the exact mechanism and factors that influence the catalytic activity and selectivity of Cu electrodes for CO_2 reduction are not fully understood. However, some relevant progress has been made. In this sense, Schouten et al.,[14,22] have recently reported the effects of the pH and the surface structure. In addition, the effects of oxide species and roughness of the electrode have been also reported.[18,23,24] DFT calculations have also shown that for metal surfaces, the reaction step in which adsorbed CO is reduced is rather insensitive with respect to CO binding energy; [25] however it depends on the surface coverage of the CO adsorbed.

View Article Online
DOI: 10.1039/C5TA06804E

It has also been suggested that the adsorbate-induced local charge might influence the adsorption energy of different intermediate species. [26]

In the past decade, the lattice mismatch between the metal overlayer and the substrate has been used as a common strategy in electrocatalysis to tune the adsorption energies of the reactive and/or intermediate surface species[27,28]. This strategy has been also recently applied to the optimization of a catalyst for CO_2 electroreduction. Thus, Plana et al.[10] have reported the effect of Pd overlayer growth on Au nanoparticles on CO_2 reduction, while Varela et al.[12] and Reske et al.[13] have explored the growth of Cu overlayers on Pt electrodes. In these studies, the authors concluded that the catalyst with overlayers showed higher catalytic activity than the pure metal catalyst and, also, that a correspondence exists between the thickness of the overlayers and the catalyst's activity and selectivity. DFT calculation and UHV experiments have shown that the H_2 adsorption and dissociation, and the adsorption of oxygen on Cu surfaces, depend not just on the surface structure, but also on the tensile strain of the Cu surface. [29-31]

On the other hand, Friebel et al. have reported the electronic and structural effects of growing Cu monolayers on Au(111) single crystal electrodes.[32] In their work, the authors showed how the strain of a single monolayer of Cu on Au electrodes affects the redox potentials of Cu. The authors suggested that the strain might also affect the catalytic activity and selectivity of the catalyst towards CO_2 reduction through the formation of different intermediate species, although these experiments have not been performed yet. Based on this premise, and considering that Cu(100) electrodes show high selectivity towards the reduction of CO_2 [14,16] we will explore, in this work, the effect of Cu overlayer growth on cubic Au nanoparticles towards the electrochemical reduction of CO_2.

2. Experimental Procedure

Synthesis of cubic gold nanoparticles

Cubic nanoparticles were synthetized by a colloidal seed-mediated method, using spherical gold nanoparticles as seeds and following the experimental procedure described by Sau and Murphy[33] and described in detail in the supporting information.

Prior to the formation of the Cu layers, the nanoparticles solution was centrifuged for 30 min at 3000 rpm to remove excess of reactants. The precipitate was collected and re-dispersed in 2mL of ultrapure water.

Synthesis of Au@Cu nanoparticles

The Au@Cu nanoparticles were prepared by modifying the procedure described by Kuo et al[34]. In a 60 mL polystyrene vial, the following were mixed together for 4 h at 40 °C: 9.4 mL of ultrapure water, 0.1 mL of a 10^{-3} M $CuCl_2$ (Aldrich 97%) solution and 0.087 g of sodium dodecyl sulfate (SDS,

View Article Online
DOI: 10.1039/C5TA06804E

Sigma Aldrich 92.5-100%). Then, 0.25 mL of a 1 M NaOH (99.99 %, Sigma-Aldrich) solution was added. The solution was kept at 40 °C and under external mixing for 2 h.

The different Au@Cu nanoparticles were prepared by adding different volumes of the Au nanoparticle solution. After 2 h, 200 μL (Au@Cu1), 150 μL (Au@Cu2) and 50 μL (Au@Cu3) were added respectively, and the resulting solutions were mixed for 2 h. Finally, 0.15 mL of a freshly prepared 0.2 M solution of NH_2OHCl (Sigma-Aldrich, Reagent plus 99%) was added under vigorous mixing. Adding the reducing agent slowly results in samples with larger particle size distribution. The reaction was considered complete after 3 hours. The samples were characterized by UV-Vis and then cleaned for further characterization and electrochemical measurements.

To collect the products, the nanoparticle solutions were washed 4 times, first with ethanol (Fisher Scientific, analytical grade and centrifuged at 3000 rpm for 10 min) and then another 3 times with ultrapure water. The resulting solution of nanoparticles was re-dispersed in 2 mL ultrapure water.

Characterization of the nanoparticles

Transmission Electron Microscopy (TEM) was performed using a Jeol 2100 LaB6 TEM instrument. Ethanolic suspensions of each catalyst were drop-casted on carbon-coated copper grids and then air-dried until complete solvent evaporation.

High angle annular dark field scanning-transmission electron microscopy (HAADF SEM) images were recorded using a Jeol 2100F STEM.

X-ray diffraction (XRD) patterns were obtained with a Bruker AXS D2 PHASER diffractometer using CoKα (0.179 nm) radiation. Samples were prepared by depositing a couple of drops (20 μL) on a quartz holder and allowing the drops to air-dry.

X-ray fluorescence spectra were obtained using a Bruker S8 Tiger spectrometer. UV−vis absorption spectrums were measured using a Cary 50 spectrophotometer, 70 μL disposable cuvettes, and a path length of 1cm.

Electrochemical measurements

A two-compartment electrochemical cell was employed, a gold wire was used as a counter electrode and a Hg/HgO electrode was used as reference electrode. All the graphs are presented in a reversible hydrogen electrode (RHE) scale. Electrochemical measurements were performed with an Autolab PGSTAT12. The phosphate buffer solution (pH=8; 94 mL of 1 M K_2HPO_4 + 6 mL of 1 M KH_2PO_4) were prepared from Sigma-Aldrich ACS reagent chemicals, >98% and >99.0%, respectively, and ultra-pure water (Elga PureUltra, 18.2 MΩ cm, 1 ppb total organic carbon). Argon (Ar, (N66)) was used to deoxygenate all solutions and CO_2 (BOC) was used to saturate the solutions. Au and Au@Cu nanoparticles were deposited on a glassy carbon rod (SIGRADUR) electrode with 2.0 mm diameter. The electrode was polished with diamond alumina before each experiment. All the measurements

View Article Online
DOI: 10.1039/C5TA06804E

were performed under steady state conditions and the cyclic voltammograms correspond to the first cycle. The uncompensated solution resistance (28 Ω) was measured by using the positive feedback mode of the potenciostat and all the cyclic voltammetries were corrected by the solution resistance.

On-line electrochemical mass spectrometry

On-line Electrochemical Mass Spectrometry (OLEMS) was used to detect the gaseous products formed during the reaction. The reaction products at the electrode interface were collected with a small tip positioned close to the electrode. The tip is a 1mm diameter porous Teflon cylinder (Porex with an average pore size of 5 μm - 10 μm and 45% - 55% porosity) in a Kel-F holder. The tip configuration was cleaned overnight in a 2 M NaOH solution (VWR, EMSURE) and rinsed 5 times with ultrapure warm water before use. A secondary electron multiplier (SEM) voltage of 1329 V was used, except for hydrogen (m/z = 2) where a SEM voltage of 2100 V was used. The pressure was equilibrated for 1 h prior to each measurement.

On-line HPLC

Soluble reaction products were detected with on-line high-performance liquid chromatography (HPLC).[35] While changing the potential from 0 V to -1.5 V vs RHE, samples of the electrolyte were collected with an open tip, which was positioned close to the centre of the electrode surface. Samples were collected with a rate of 60 μL min^{-1} and each sample had a volume of 60 μL. Since the potential was changed at 1 mVs^{-1}, each sample contained the average reaction products of a potential change of 60 mV. Samples collected during voltammetry were analyzed afterwards by HPLC (Prominence HPLC, Shimadzu, Aminex HPX 87-H column, Biorad). The separated compounds were detected with a refractive index detector (RID-10A).

3. Results and Discussion

Figure 1a-b shows some representative transmission electron microscopy (TEM) images of the cubic gold nanoparticles prepared by the method described in the experimental section. As can be seen, the nanoparticles are uniform in shape and size (40 ± 2 nm). The inset on figure 1b shows the electron diffraction pattern obtained by directing the electron beam perpendicular to one of the square faces of the cube. The square symmetry of this pattern indicates that each gold nanocube was a single crystal mainly bounded by (100) facets. This fact was also confirmed by XRD (Figure SI4).

After successive steps, as described in the experimental section, the cubic Au nanoparticles were coated with Cu overlayers of different thickness. The UV-vis absorption spectral results of these Au-Cu samples (Figure 2) provide strong evidence that all the gold nanocrystals have turned into core−shell Au@Cu nanoparticles. The absorption bands of the core shell nanoparticles show a shift towards the red region due to the large particle sizes in comparison with the bare gold nanocrystals (maximum absorption at ~535 nm).[36,37] As can be seen from the TEM images in Figures 1c-1f , the

View Article Online
DOI: 10.1039/C5TA06804E

samples Au@Cu1 (6-7 Cu layers) and Au@Cu2 (14-16 Cu layers) show an increase of the particles size while maintaining a cubic shape. On the other hand, Au@Cu3 (30-40 Cu layers) shows an increase of size and, even though the nanoparticles show 90° angles associated with (100) sites, the nanoparticles became almost spherical (see Figure 1g, 1h). Although several attempts were carried out, we have not been able to prepare Cu shells of more than 20 layer with (100) preferential orientation. High angle annular dark field scanning transmission electron microscopy (HAADF STEM) images (Figure 1f and 1h (inset)) allow the Au cubic core to be clearly identified. This Au core is much brighter than that of the Cu shell on the Au@Cu2 and Au@Cu3 samples, as a consequence of the higher atomic number of gold (Z = 79) than that of copper (Z = 29).

The atomic composition of the nanoparticles was determined by electrochemical methods (Figure 3) and confirmed by X-ray fluorescence (XRF) (Figure SI5). Figure 3A shows cyclic voltammograms of the Au@Cu nanoparticles in a 0.1 M H_2SO_4 electrolyte. The electrochemical response can be separated into two well-defined regions – the first region between 0.3 V and 0.5 V and the second region between 0.5 V and 0.8 V. As can be seen in the positive scan, the increase in the number of Cu layers results in an increase of charge in both regions; however the region at higher potentials shows a large increase of charge. While the shape of the voltammetric profiles of Au@Cu1 and Au@Cu2 are similar to that of the expected Cu UPD on gold, the voltammetric profile of Au@Cu3 resembles the profile of the bulk oxidation of Cu in sulphuric acid.[38] Previous results regarding the underpotential deposition of Cu on gold electrodes in sulphuric acid have attributed the two different potential processes to two different oxidation steps. The negative scan in the voltammetry shows the reduction of the Cu oxides formed on the surface. As can be seen, while Au@Cu1 shows a single peak located at 0.40 V, Au@Cu2 shows two distinctive signals at 0.47 V and 0.52 V. This latter contribution is also present for Au@Cu1, but only as a small shoulder. Grishina et al. associate the peak at lower potentials to the reduction of Cu_2O, while the peak at higher potentials corresponds to the reduction of CuO.[38] This observation is also in agreement with those results presented by Friebel et al. for monolayers of Cu on gold single crystal electrodes and therefore, we can extrapolate those findings to the Cu layers on the cubic gold nanoparticles[32].

Figure 3B shows the step-potential dissolution of Cu at 0.85 V vs RHE from the Au@Cu nanoparticles. The chronoamperometry of Au@Cu1 shows a single signal associated with the dissolution of copper. Interestingly, this signal shifts as the number of Cu layers increases, indicating an easier dissolution of copper at this higher potential. In addition, on Au@Cu3, a second signal appears at longer times. Vogt et al. proposed that the dissolution rate of Cu(100) in sulphuric acid depends strongly on the surface morphology of the adlayer structure,[39] therefore the two dissolution signals observed in the chronoamperometry must be associated with two different surface structures induced by the lattice strain. The dissolution charge was determined by integrating the I-t signal of the chronoamperometry in Figure 3B. Table 1 summarizes the mass composition obtained from the XRF

View Article Online
DOI: 10.1039/C5TA06804E

spectra and the charge associated to the dissolution of the Cu layers as determined by chronoamperometry. Based on the values of Table 1 and assuming a constant particle size of 40 nm, the number of Cu layers for each of the samples was determined. As can be seen, the number of layers is in good agreement with the thickness of the Cu layers as determined by TEM (Figure 1).

Figure 4 shows the voltammetric profiles of the Au and Au@Cu nanoparticles in phosphate buffer solution (PBS, pH=8) both in absence and presence of CO_2. As can be seen from figure 4A, hydrogen evolution reaction takes place at less negative potentials on the gold nanoparticles [40-42]. The onset of the HER is shifted towards more negative potentials as a function of the number of Cu layers.

We also consider the Au and Au@Cu nanoparticles in a CO_2 saturated solution and observe that the electrochemical behaviour is significantly different. The first observation is that the overpotential of the CO_2 reduction on the Au@Cu1 and Au@Cu2 samples is lower than that of the Au nanoparticles (up to 200 mV). This trend is in agreement with the results reported by Hori et al. who showed that the onset potential for the CO_2 reduction on Cu bulk electrodes is lower than the onset potential of Au bulk electrodes.[43] Xu et al. also who showed that the onset potential for the CO_2 reduction on for AuCu alloy nanoparticles appears at lower potentials than on Au nanoparticles.[11] Interestingly, and despite the difference in the blank voltammetry, the voltammetric profiles of Au@Cu1 and Au@Cu2 are similar in both their onset potential and their current densities. On the other hand, the onset potential for the CO_2 reduction on Au@Cu3 nanoparticles is shifted towards more negative potentials. This might be attributed to changes in the surface structure. As it was mentioned before, from Figure 1g and 1h, it is possible to conclude that the Au@Cu3 nanoparticles presented significant differences of surface structure when compared with the Au@Cu1 and Au@Cu2 nanoparticles. The Cu layers appear to grow epitaxially on Au@Cu1 and Au@Cu2; therefore, the domains are (100). The Au@Cu3 presents round edges and also 60 ° angles between the facets and therefore are more likely to be associated to (111) facets and step sites. These changes in surface structure might lead to different reactivity. [14] Another interesting observation is that the samples Au, Au@Cu1 and Au@Cu2 (lower amount of copper) present larger deactivation (lower currents in the negative-going scan) when compared with Au@Cu3. This electrochemical behaviour might suggest the formation of different intermediate adsorbed species and products. It has been recently suggested by Shi et al. that CO_2 reactivity for strong-binding metals depends on the surface coverage of CO adsorbed species and thus the hydrogen evolution reaction. The authors have also concluded that, on the strong-binding metals, the selectivity towards the formation of the *COH intermediate over the *CHO intermediate decreases as the CO adsorbed species increases. The authors also concluded that the adsorbate–adsorbate interactions push the thermodynamics to slightly favour the formation of the *CHO intermediate. [26]

Figure 5 shows the gaseous product distribution for the reduction of CO_2 during the cyclic voltammetry, as determined by on-line electrochemical mass spectrometry. As can be seen, the formation of the reaction products starts as early as -0.3 V vs RHE. The formation of hydrogen

View Article Online
DOI: 10.1039/C5TA06804E

product is quite similar for the three Au@Cu samples and the small differences are within experimental error. However, the formation of methane and ethane is clearly dependent on the number of Cu layers and the applied potential. In the potential region between -0.35 V and -0.6 V vs RHE, Au@Cu1 shows a larger formation of ethylene; while, in the same potential region, Au@Cu2 is more selective towards the formation of methane. Interestingly, at higher overpotentials (from -0.6 V to -0.8 V) Au@Cu1 produces more methane; while, Au@Cu2 is more selective towards the formation of ethylene. It is also important to highlight that the Au@Cu1, the one having the lowest Cu amount deposited on the (100) enriched cubic gold nanoparticles, has a product selectivity as a function of the potential similar to that observed on Cu(100) at pH=7 [14]. On the other hand, the sample Au@Cu3 presents a similar behaviour to that observed by Kortlever et al. for Cu polycrystalline electrodes at pH 6.7, at which the formation of methane and ethane appears at around -0.8 V vs RHE.[44]

Together with the gaseous distribution, we have also determined the formation of liquid products by using on-line HPLC. Formic acid was the only liquid species observed during the CO_2 reduction and it is observed at potentials below -0.7 V vs RHE (Figure 6). As can be seen, the formation of formic acid is strongly dependent on the number of Cu layers on the core@shell nanoparticles. Among the Au@Cu samples, the Au@Cu3 showed the smallest amount of formic acid, which was only detected at potentials below -1 V vs RHE.

By comparison, the formation of formic acid on Au@Cu1 appears at around -0.75 V vs RHE while the Au@Cu2 starts at slightly higher overpotentials (-0.85 V).[44] Even though the onset potential for the formation of formic acid is similar, the concentration of formic acid is significantly higher on the Au@Cu1 when the applied potential is more negative than -0.95 V. The concentration of formic acid per surface mass on the Au@Cu2 at -1 V vs RHE is 13 mM/mg. Remarkably, the maximum concentration of formic acid per mass of catalyst produced by the Au@Cu1 at -1 V vs RHE was 45 mM/mg.

As it was described before, the voltammetric profiles of Au, Au@Cu1 and Au@Cu2 present significantly lower current densities on the negative-going scan when compared with the positive-going scan. This might suggest the formation of intermediate poisoning species and therefore the catalytic activity and product distribution might change over time. In order to determine the relative gas product distribution over time, chronoamperometries at -0.6 V vs RHE were performed for one hour in combination with OLEMS measurements (Figure 7). To provide a semi-quantitative analysis of the product distribution in the gas phase, the y-coordinates are presented as the ratio between the partial pressure of the products and the total pressure of the products[45]. The total pressure of the products in each case was obtained by subtracting the changes in the water partial pressure (m/z=18) and the signal of the CO_2 (m/z= 44) from the total pressure of the system. An example of the total pressure, the water partial pressure and the CO_2 signal is presented in figure SI3. The first observation is the good stability in the product formation of H_2 on the sample Au@Cu3; whereas, the samples

View Article Online
DOI: 10.1039/C5TA06804E

Au@Cu1 and Au@Cu2 show a significant decrease in the hydrogen formation over time. Interestingly, Au@Cu3 shows an increase in the formation of methane over time; while, at the same time, the formation of ethylene decreases to zero after 2500 s. The sample Au@Cu1 shows decay in the production of hydrogen during the first 2000 s while the formation of CH_4 can be consider stable during the entire hour with just minor variations. An increase in the formation of C_2H_4 was observed over time. On the other hand, Au@Cu2 shows an initial decay in the production of hydrogen while the reduction of CO_2 to methane and ethylene is almost constant during the entire hour. In the case of the Au nanoparticles, just hydrogen formation was observed as shown in figure SI6, however the partial pressure of the hydrogen correspond just to about 20% of the total pressure after the subtraction of the CO_2 and water partial pressure contributions which means that about 80% of the total pressure corresponds to the formation of other gaseous products not detected. It is well-described that Au electrodes show efficiencies between 80-95% for the reduction of CO_2 to CO [46-48].

Figure 8 shows the total gas product distribution accumulated during the chronoamperometry measurement (figure 7). As can be seen, over time, Au@Cu1 presents higher selectivity towards the formation of hydrogen and ethylene, while Au@Cu2 and Au@Cu3 are more selective towards the formation of hydrogen and methane. A trend in the formation of the gaseous products can be also drawn. The H_2 and CH_4 formation increases with the number of Cu layers, while the formation of ethylene decreases.

In the case of the Au@Cu1 and Au@Cu2, we may attribute the differences in the product distribution to the strain effect of the Cu overlayer in the adsorption of reactive intermediate species due to different structural and electronic effects. Based on the product selectivity of the cyclic voltammetry, the Cu electrode (Au@Cu1) favours the formation of C-C bonds and by increasing the number of Cu overlayers, the hydrogenation pathway of the CO_2 to CH_4 is promoted. This is similar to the finding regarding Cu overlayers on Pt.[13] Unfortunately, this conclusion cannot be fully extrapolated to the sample Au@Cu3 since other effects might be playing a role in the product distribution (surface structure, roughness[24] and inclusive a significantly larger particle size[49]). As discussed above, the voltammetry experiments are evidence of the different surface energies of the Cu layers on the three samples. These electronic effects might play an important role in the adsorption energy of the intermediate species during CO_2 reduction.

We have shown using chronoamperometry experiments that the gas product selectivity is time-dependent. Nevertheless, the reason behind this still requires further studies. A tentative explanation is the formation of poisoning species [3] and the change of the surface structure due to Cu surface diffusion or copper brightening[50,51]. Some indications on the change of the surface structure of copper have been very recently reported by Kim et al. using electrochemical STM[52]. In that work the authors showed how a polycrystalline copper electrode undergoes surface reconstruction at negative potentials in alkaline medium. On the other hand, previous DFT calculations for the hydrogen adsorption on Cu

View Article Online
DOI: 10.1039/C5TA06804E

surfaces have shown that an upshift of the surface d-band centre takes place on Cu surfaces upon lattice expansion. According to the *d*-band model, this leads to a stronger atomic binding and to smaller dissociation barriers on the expanded Cu surfaces. [30] However, the tensile strain of the layers depends on the number of layers. Kongstein et al. have shown tensile-compressive transition when Cu layers are grown on Au(111) electrodes. The author showed that, within the first 20 nm of bulk Cu deposition, there is a rapid increase in tensile stress ascribed to nuclei coalescence and grain boundary formation. When the films become continuous, the stress becomes compressive. It is important to note that the hydrogen evolution presented different kinetics as a function of the number of Cu layers. [53]

Sakong et al. has also shown that the trend of hydrogen adsorption and dissociation probability as a function of the lattice strain also strongly depends on the adsorption of other species (e.g., oxygen). [30] They have proposed that adsorbate-induced changes of the Cu local *d*-band density of states have to be taken into account in order to rationalise the adsorption energies of hydrogen. Similarly, the adsorbed-induced charge effect has been described for the cooperative adsorption of CO and OH on Au(111) surfaces. [54] More recently, Shi et al. has also shown that the interactions between adsorbed CO and intermediates in both the hydrogen evolution reaction (HER) and the CO_2 reduction reaction (CO_2RR) are important. [26]

4. Acknowledgement

P.R. acknowledges the Veni grant for partial financial support of this project. P.R. would also like to acknowledge the University of Birmingham for the financial support through the Birmingham fellowship program. P.R. and J.M acknowledges Dr. Daniela Plana, Jo Humphrey and Jonathan Jones and the Centre for Electron Microscopy of the University of Birmingham for the support in the utilization of the microscopy facilities at the University of Bristol and the University of Birmingham, J.M. acknowledges the University of Birmingham for the financial support through PhD scholarships at the School of Chemistry.

5. References

(1) Organization, W. M. *WMO GREENHOUSE GAS BULLETIN* **2014**, 8.
(2) Kondratenko, E. V.; Mul, G.; Baltrusaitis, J.; Larrazabal, G. O.; Perez-Ramirez, J. *Energy & Environmental Science* **2013**, *6*, 3112.
(3) Peterson, A. A.; Abild-Pedersen, F.; Studt, F.; Rossmeisl, J.; Norskov, J. K. *Energy & Environmental Science* **2010**, *3*, 1311.
(4) Li, K.; An, X.; Park, K. H.; Khraisheh, M.; Tang, J. *Catalysis Today* **2014**, *224*, 3.
(5) B.C.Brodie In *Procedings of the Royal Society* London, 1873; Vol. XX, p 245.
(6) Hori, Y.; Koga, O.; Aramata, A.; Enyo, M. *Bulletin of the Chemical Society of Japan* **1992**, *65*, 3008.
(7) Hoshi, N.; Suzuki, T.; Hori, Y. *Journal of Electroanalytical Chemistry* **1996**, *416*, 61.

View Article Online
DOI: 10.1039/C5TA06804E

(8) Hoshi, N.; Noma, M.; Suzuki, T.; Hori, Y. *Journal of Electroanalytical Chemistry* **1997**, *421*, 15.

(9) Lu, Q.; Rosen, J.; Zhou, Y.; Hutchings, G. S.; Kimmel, Y. C.; Chen, J. G.; Jiao, F. *Nat Commun* **2014**, *5*.

(10) Plana, D.; Florez-Montano, J.; Celorrio, V.; Pastor, E.; Fermin, D. J. *Chemical Communications* **2013**, *49*, 10962.

(11) Xu, Z.; Lai, E.; Shao-Horn, Y.; Hamad-Schifferli, K. *Chemical Communications* **2012**, *48*, 5626.

(12) Varela, A. S.; Schlaup, C.; Jovanov, Z. P.; Malacrida, P.; Horch, S.; Stephens, I. E. L.; Chorkendorff, I. *The Journal of Physical Chemistry C* **2013**, *117*, 20500.

(13) Reske, R.; Duca, M.; Oezaslan, M.; Schouten, K. J. P.; Koper, M. T. M.; Strasser, P. *The Journal of Physical Chemistry Letters* **2013**, *4*, 2410.

(14) Schouten, K. J. P.; Pérez Gallent, E.; Koper, M. T. M. *Journal of Electroanalytical Chemistry* **2014**, *716*, 53.

(15) Montoya, J. H.; Peterson, A. A.; Nørskov, J. K. *Chemcatchem* **2013**, *5*, 737.

(16) Calle-Vallejo, F.; Koper, M. T. M. *Angewandte Chemie International Edition* **2013**, *52*, 7282.

(17) Hatsukade, T.; Kuhl, K. P.; Cave, E. R.; Abram, D. N.; Jaramillo, T. F. *Physical Chemistry Chemical Physics* **2014**, *16*, 13814.

(18) Kas, R.; Kortlever, R.; Milbrat, A.; Koper, M. T. M.; Mul, G.; Baltrusaitis, J. *Physical Chemistry Chemical Physics* **2014**, *16*, 12194.

(19) Zhu, W.; Michalsky, R.; Metin, Ö.; Lv, H.; Guo, S.; Wright, C. J.; Sun, X.; Peterson, A. A.; Sun, S. *J. Am. Chem. Soc.* **2013**, *135*, 16833.

(20) Kim, D.; Resasco, J.; Yu, Y.; Asiri, A. M.; Yang, P. *Nat Commun* **2014**, *5*.

(21) Kuhl, K. P.; Hatsukade, T.; Cave, E. R.; Abram, D. N.; Kibsgaard, J.; Jaramillo, T. F. *J. Am. Chem. Soc.* **2014**, *136*, 14107.

(22) P. Schouten, K. J.; Gallent, E. P.; Koper, M. T. M. *Journal of Electroanalytical Chemistry* **2013**, *699*, 6.

(23) Le, M.; Ren, M.; Zhang, Z.; Sprunger, P. T.; Kurtz, R. L.; Flake, J. C. *Journal of the Electrochemical Society* **2011**, *158*, E45.

(24) Kas, R.; Kortlever, R.; Yılmaz, H.; Koper, M. T. M.; Mul, G. *ChemElectroChem* **2014**, n/a.

(25) Peterson, A. A.; Nørskov, J. K. *The Journal of Physical Chemistry Letters* **2012**, *3*, 251.

(26) Shi, C.; Hansen, H. A.; Lausche, A. C.; Norskov, J. K. *Physical Chemistry Chemical Physics* **2014**, *16*, 4720.

(27) Kitchin, J. R.; Norskov, J. K.; Barteau, M. A.; Chen, J. G. *Physical Review Letters* **2004**, *93*.

(28) Strasser, P.; Koh, S.; Anniyev, T.; Greeley, J.; More, K.; Yu, C.; Liu, Z.; Kaya, S.; Nordlund, D.; Ogasawara, H.; Toney, M. F.; Nilsson, A. *Nature Chemistry* **2010**, *2*, 454.

(29) Álvarez-Falcón, L.; Viñes, F.; Notario-Estévez, A.; Illas, F. *Surface Science*.

(30) Sakong, S.; Groß, A. *Surface Science* **2003**, *525*, 107.

(31) Uesugi-Saitow, Y.; Yata, M. *Physical Review Letters* **2002**, *88*, 256104.

(32) Friebel, D.; Mbuga, F.; Rajasekaran, S.; Miller, D. J.; Ogasawara, H.; Alonso-Mori, R.; Sokaras, D.; Nordlund, D.; Weng, T.-C.; Nilsson, A. *The Journal of Physical Chemistry C* **2014**, *118*, 7954.

(33) Sau, T. K.; Murphy, C. J. *J. Am. Chem. Soc.* **2004**, *126*, 8648.

(34) Kuo, C.-H.; Hua, T.-E.; Huang, M. H. *J. Am. Chem. Soc.* **2009**, *131*, 17871.

(35) Kwon, Y.; Koper, M. T. M. *Analytical Chemistry* **2010**, *82*, 5420.

(36) Alvarez-Paneque, A. F.; Rodríguez-González, B.; Pastoriza-Santos, I.; Liz-Marzán, L. M. *The Journal of Physical Chemistry C* **2012**, *117*, 2474.

View Article Online
DOI: 10.1039/C5TA06804E

(37) Tsuji, M.; Yamaguchi, D.; Matsunaga, M.; Alam, M. J. *Crystal Growth & Design* **2010**, *10*, 5129.
(38) Grishina, E. P.; Udalova, A. M.; Rumyantsev, E. M. *Russian Journal of Electrochemistry* **2002**, *38*, 1041.
(39) Vogt, M. R.; Lachenwitzer, A.; Magnussen, O. M.; Behm, R. J. *Surface Science* **1998**, *399*, 49.
(40) Quaino, P.; Juarez, F.; Santos, E.; Schmickler, W. *Beilstein Journal of Nanotechnology* **2014**, *5*, 846.
(41) Frese, U.; Stimming, U. *Journal of Electroanalytical Chemistry and Interfacial Electrochemistry* **1986**, *198*, 409.
(42) Trasatti, S. *Journal of Electroanalytical Chemistry and Interfacial Electrochemistry* **1972**, *39*, 163.
(43) Hori, Y.; Wakebe, H.; Tsukamoto, T.; Koga, O. *Electrochimica Acta* **1994**, *39*, 1833.
(44) Kortlever, R.; Tan, K. H.; Kwon, Y.; Koper, M. T. M. *J Solid State Electrochem* **2013**, *17*, 1843.
(45) Gervasini, G. 2015; Vol. 2015.
(46) Christophe, J.; Doneux, T.; Buess-Herman, C. *Electrocatalysis* **2012**, *3*, 139.
(47) Stevens, G. B.; Reda, T.; Raguse, B. *Journal of Electroanalytical Chemistry* **2002**, *526*, 125.
(48) Chen, Y.; Li, C. W.; Kanan, M. W. *J. Am. Chem. Soc.* **2012**, *134*, 19969.
(49) Reske, R.; Mistry, H.; Behafarid, F.; Roldan Cuenya, B.; Strasser, P. *J. Am. Chem. Soc.* **2014**, *136*, 6978.
(50) Matsushima, H.; Haak, C.; Taranovskyy, A.; Grunder, Y.; Magnussen, O. M. *Physical Chemistry Chemical Physics* **2010**, *12*, 13992.
(51) Matsushima, H.; Taranovskyy, A.; Haak, C.; Gründer, Y.; Magnussen, O. M. *J. Am. Chem. Soc.* **2009**, *131*, 10362.
(52) Kim, Y.-G.; Baricuatro, J. H.; Javier, A.; Gregoire, J. M.; Soriaga, M. P. *Langmuir* **2014**, *30*, 15053.
(53) Kongstein, O. E.; Bertocci, U.; Stafford, G. R. *Journal of the Electrochemical Society* **2005**, *152*, C116.
(54) Rodriguez, P.; Kwon, Y.; Koper, M. T. M. *Nat Chem* **2012**, *4*, 177.

Tables

Table 1. Calculated mass, dissolution charge and thickness of the copper layers on Au cubic nanoparticles.

	X-ray fluorescence		Electrochemical methods	
Sample	**% Cu**	**# Cu layers**	**Chronoamperometry Q/μC**	**# Cu layers**
Au@Cu1	19.1±1.2	9-10	314.3	7-8
Au@Cu2	30.2±1.5	17-18	605.1	14-16

View Article Online
DOI: 10.1039/C5TA06804E

Au@Cu3	48.6±1.7	35-40	1212	30-40

Figure Caption

Figure 1. TEM images of Au cubic nanoparticles (a (scale bar =500 nm), b(scale bar =50 nm)), Au@Cu1 core@shell nanoparticles (c(scale bar =50 nm), d (scale bar =10 nm)), Au@Cu2 core@shell nanoparticles (e(scale bar =100 nm), f(scale bar =50 nm)) and Au@Cu3 core@shell nanoparticles (g(scale bar =100 nm), h(scale bar =50 nm)). The inset on figure b corresponds to the electron diffraction pattern of a single Au cubic nanoparticle (scale bar =1 nm). The inset in figures f (scale bar =2nm) and h (scale bar =15 nm) corresponds to the HAADF STEM images of the Au@Cu2 and Au@Cu3 nanoparticles, respectively. Bright zone correspond to the Au core (Z =79) while darker zones correspond to the Cu shell (Z =29).

View Article Online
DOI: 10.1039/C5TA06804E

Figure 2. UV Vis absorption spectra and absorption shift of Au (black line), Au@Cu1 (red line), Au@Cu2 (blue line) and Au@Cu3 (green line) nanoparticles. The inset corresponds to the optical image of the 4 samples.

Figure 3. Voltammetric profiles (A) and potential step chronoamperometry 0.3V →0.85V vs RHE (B) of Au@Cu1 (red line), Au@Cu2 (blue line) and Au@Cu3 (green line) nanoparticles in 0.1 M H_2SO_4. Scan rate in (A) υ= 10 mV s^{-1}.

Figure 4. Cyclic voltammograms of Au (black line), Au@Cu1 (red line), Au@Cu2 (blue line) and Au@Cu3 (green line) nanoparticles in (A) PBS (pH= 8) and (B) PBS saturated with CO_2. Scan rate υ= 10 mV s^{-1}.

Figure 5. Ion currents for methane, ethylene, hydrogen probed by OLEMS as a function of applied potential for the Au@Cu1 (red curve), Au@Cu2 (blue curve) and Au@Cu3 (green curve) in CO_2 saturated PBS (pH=8) solution. Scan rate υ= 5 mV s^{-1}.

Figure 6. Concentration of formic acid determined by on-line HPLC as a function of the potential during the CO_2 reduction at Au, Au@Cu1, Au@Cu2 and Au@Cu3 nanoparticles. Scan rate υ= 1 mV s^{-1}.

Figure 7. Normalized partial pressure for methane (red curve), ethylene (green curve) and hydrogen (black curve) probed by OLEMS as a function of time for the reduction of CO_2 at -0.6 V vs RHE on the Au@Cu1, Au@Cu2 and Au@Cu3 in CO_2 saturated PBS (pH=8) solution.

Figure 8. Total gas product distribution of H_2, CH_4 and C_2H_4 on Au@Cu1 , Au@Cu2 and Au@Cu3 during the CO_2 electroreduction in PBS (pH=8) at -0.6 V vs RHE.

Figures

View Article Online
DOI: 10.1039/C5TA06804E

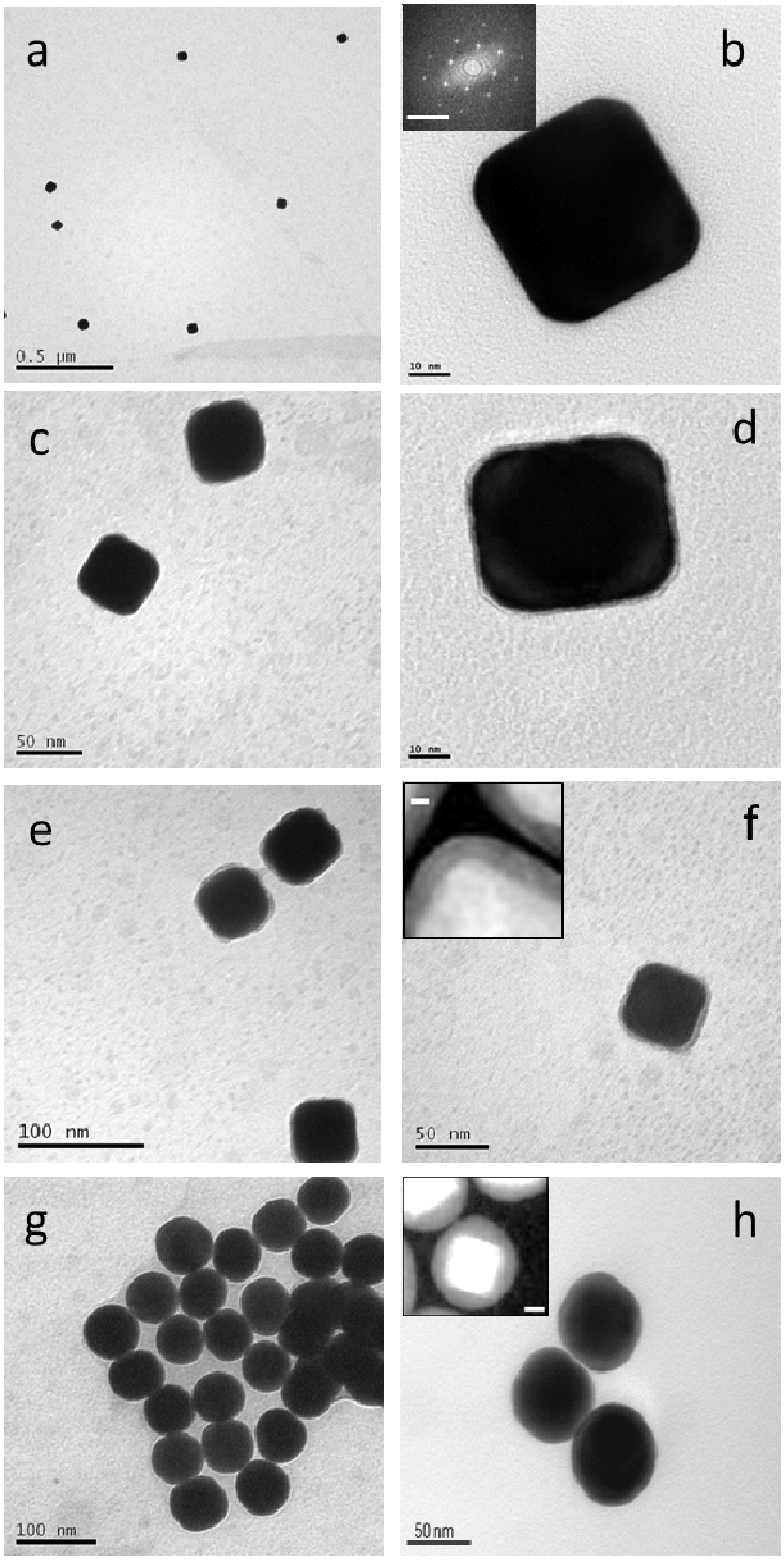

Figure 1

View Article Online
DOI: 10.1039/C5TA06804E

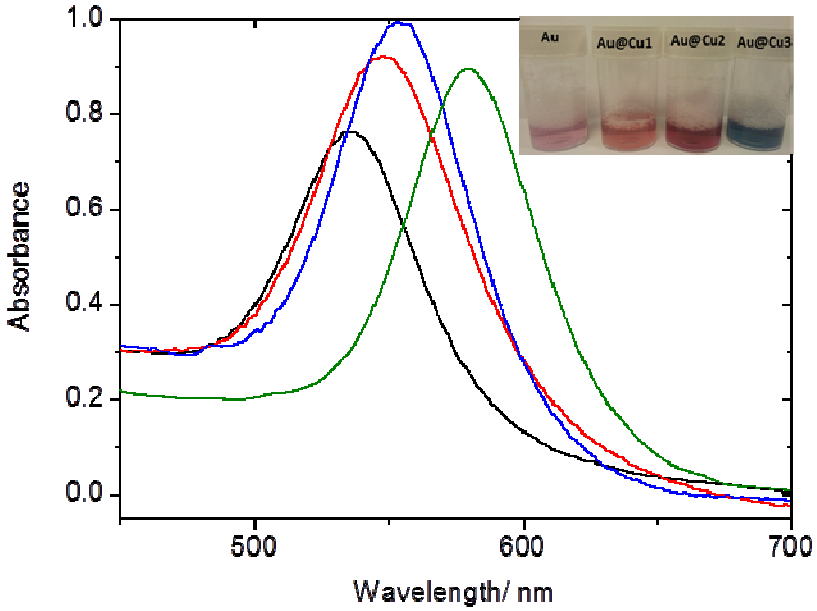

Figure 2

View Article Online
DOI: 10.1039/C5TA06804E

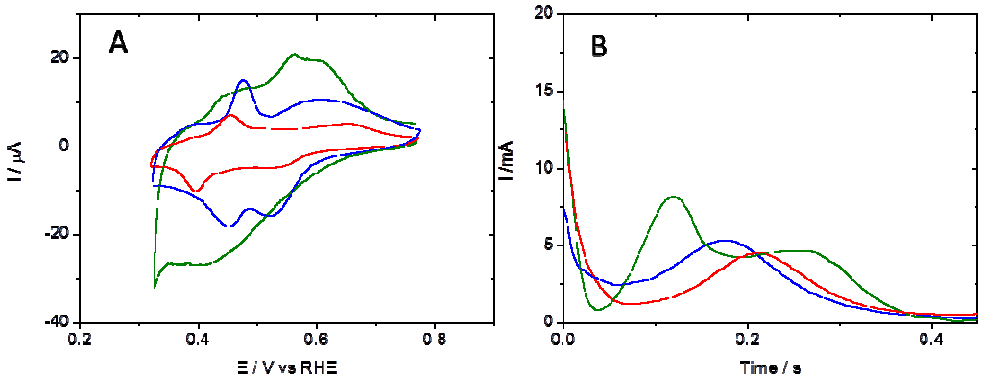

Figure 3.

View Article Online
DOI: 10.1039/C5TA06804E

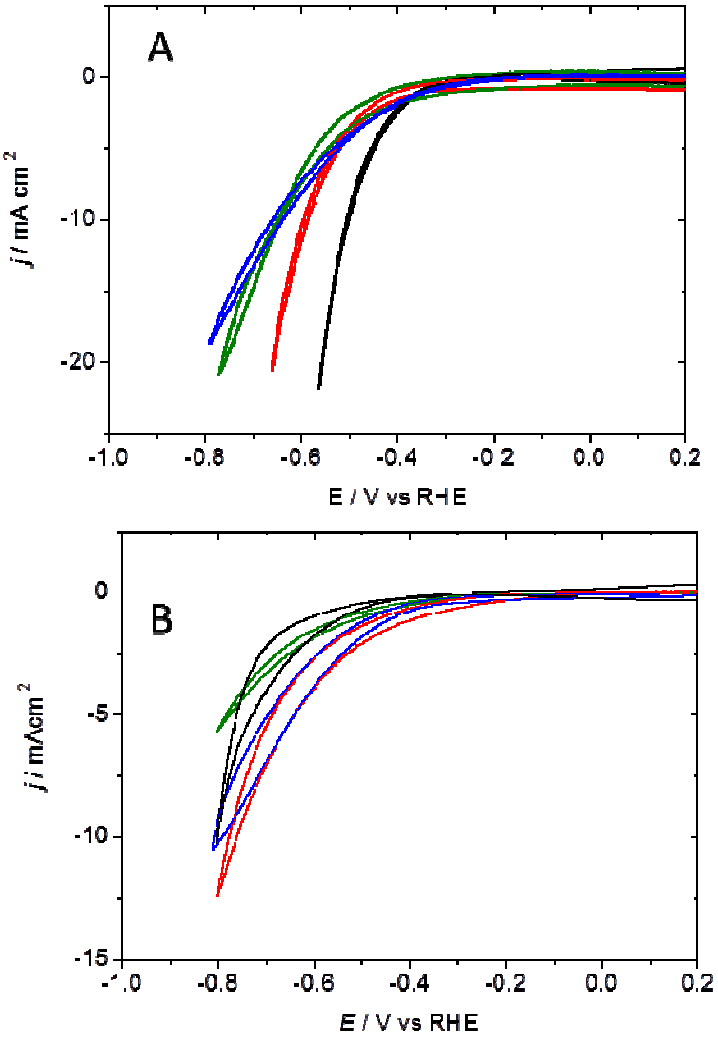

Figure 4.

View Article Online
DOI: 10.1039/C5TA06804E

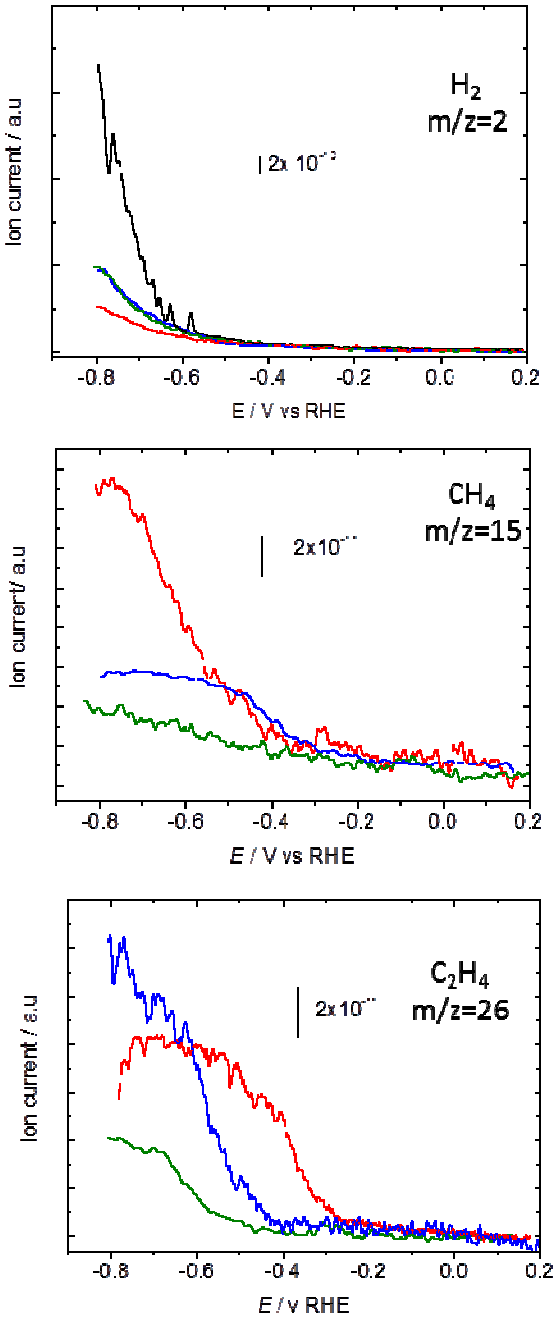

Figure 5

View Article Online
DOI: 10.1039/C5TA06804E

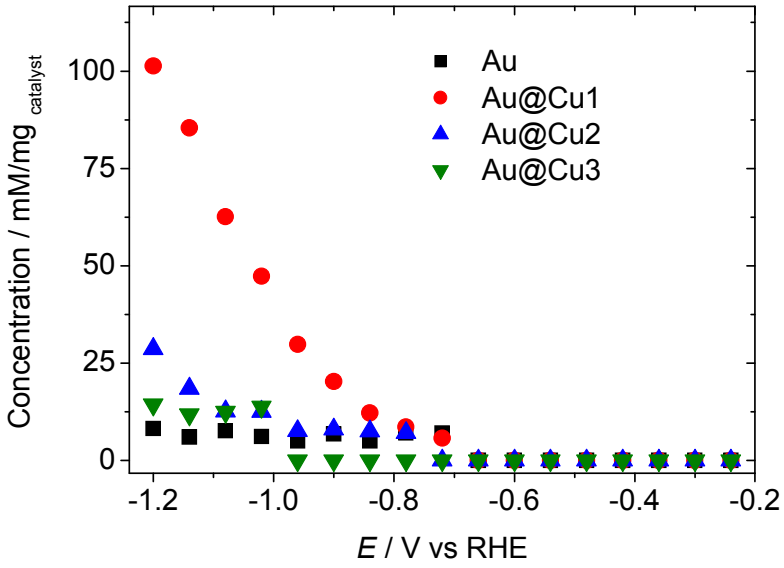

Figure 6.

View Article Online
DOI: 10.1039/C5TA06804E

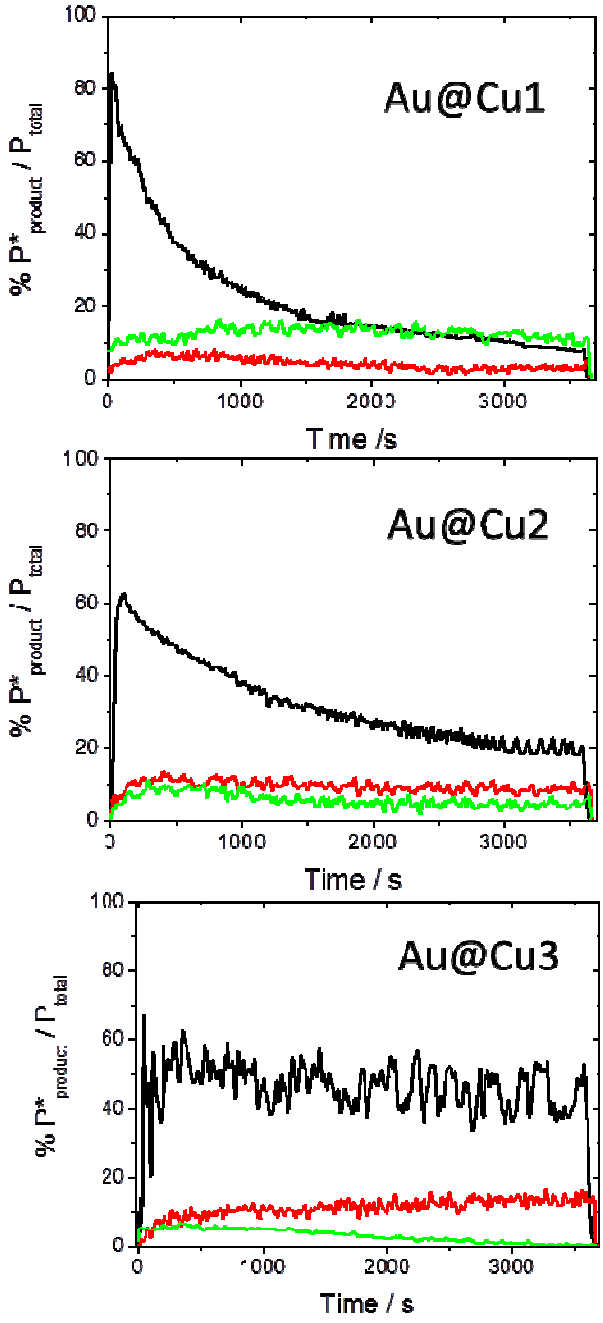

Figure 7.

View Article Online
DOI: 10.1039/C5TA06804E

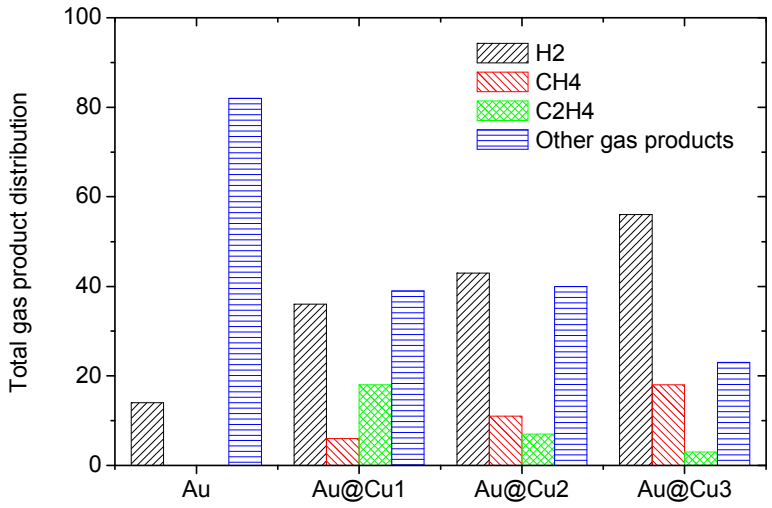

Figure 8.

View Article Online
DOI: 10.1039/C5TA06804E

Visual Abstract